Journal of Materials Chemistry C

ROYAL SOCIETY OF CHEMISTRY

PAPER

View Article Online
View Journal | View Issue

Cite this: J. Mater. Chem. C, 2020, 8, 9322

Two-site Cr^{3+} occupation in the $MgTa_2O_6:Cr^{3+}$ phosphor toward broad-band near-infrared emission for vessel visualization

Gaochao Liu,[a] Maxim S. Molokeev,[bcd] Bingfu Lei [e] and Zhiguo Xia *[a]

Received 21st April 2020,
Accepted 1st June 2020

DOI: 10.1039/d0tc01951h

rsc.li/materials-c

Near-infrared (NIR) phosphor-converted light-emitting diodes (pc-LEDs) have great potential in photonic, optoelectronic and biological applications, while the discovery of a broad-band NIR phosphor still remains a challenge. Here, we report a novel Cr^{3+}-activated $MgTa_2O_6$ phosphor with an asymmetrical emission band ranging from 700 to 1150 nm and a large full width at half maximum (FWHM) of 140 nm upon 460 nm blue light excitation. The broad spectrum is assigned to the overlap of two bands centered at 910 and 834 nm, which originate from the spin-allowed transition of $^4T_2 \rightarrow {}^4A_2$ for different Cr^{3+} ions located in the two six-coordinated crystallographic sites of Mg^{2+} and Ta^{5+}, respectively. The distribution of blood vessels and bones in human palm and wrist is observed with the assistance of a commercial NIR camera and a fabricated pc-LED, which demonstrates that the $MgTa_2O_6:Cr^{3+}$ phosphor is promising in biological applications.

1. Introduction

Near-infrared (NIR) light sources have attracted extensive attention in the fields of security, night vision and quantitative composition analysis due to their invisibility and characteristic interactions with certain biomolecules (oil, water, sugar, protein, fat, and so forth).[1–4] In particular, for the NIR radiation at 700–1100 nm, an appreciable penetration depth in biotissues makes it feasible to diagnose the physiological states of the human body harmlessly.[5–7] Thus, efficient and sustainable NIR materials used in light sources are in urgent need, especially with a wide emission spectrum to detect as many substances as possible. Various NIR luminescence materials have been developed for applications in halogen lamps, light-emitting diodes (LEDs), organic LEDs (OLEDs) and phosphor-converted LEDs (pc-LEDs). Among them, halogen lamps are characterized by their ultra-broadband spectra covering the region from the visible to the NIR region continuously, but their low luminescence efficiency, high work temperature and long response time hinder their application.[8] Although NIR LEDs overcome most of the drawbacks of halogen lamps, the narrow full width at half maximum (FWHM) of a single NIR LED (<50 nm) and the inconsistency of array LEDs also strongly restrict their large scale utilization.[9] Furthermore, emerging OLEDs display inherent flexibility and suitability for large area applications, while their efficiency and temperature resistance are disappointing.[10] In contrast, pc-LEDs seem to be a brilliant strategy due to their tunable fluorescence spectra, high radiant flux, concise fabrication technique and appreciable durability.[11–13] As a key component of the ideal pc-LEDs, broad-band NIR phosphors that can be excited by the most efficient blue LED chips should be exploited as they have become a hot topic today.

Till now, numerous NIR phosphors have been reported by introducing activators (rare earth ions, transition metal ions or Bi-ion with low valence) into inorganic host materials.[4,14–23] However, the improper NIR wavelength, narrow emission bands or the low luminescent efficiency of most dopants restrict their applications. For example, the emission wavelength of the Eu^{2+}-doped phosphor reported by our group is not long enough in the NIR region.[4] Eu^{2+}-sensitized and Nd^{3+}-activated $Sr_2Si_5N_8$ phosphors display several discontinuous sharp peaks around 900 and 1100 nm with a NIR quantum yield of 26% upon 450 nm excitation.[24] However, Cr^{3+} ions have been considered as an ideal NIR luminescent center because of their tunable emission spectra from 650 to 1600 nm and wide absorption range almost covering the entire ultraviolet–visible

[a] The State Key Laboratory of Luminescent Materials and Devices, Guangdong Provincial Key Laboratory of Fiber Laser Materials and Applied Techniques, School of Materials Science and Technology, South China University of Technology, Guangzhou 510640, P. R. China. E-mail: xiazg@scut.edu.cn
[b] Laboratory of Crystal Physics, Kirensky Institute of Physics, Federal Research Center KSC SB RAS, Krasnoyarsk 660036, Russia
[c] Siberian Federal University, Krasnoyarsk 660041, Russia
[d] Department of Physics, Far Eastern State Transport University, Khabarovsk 680021, Russia
[e] Guangdong Provincial Engineering Technology Research Center for Optical Agriculture, College of Materials and Energy, South China Agricultural University, Guangzhou 510642, P. R. China

light region.[25–28] Such excellent features of Cr^{3+} ions motivated researchers to explore appropriate luminescent materials. Rajendran *et al.* reported the ultra-broadband emission of the $La_3Ga_{4.95}GeO_{14}:Cr^{3+}$ phosphor ranging from 650 to 1200 nm with a FWHM of 330 nm.[29] In addition, Cr^{3+}-doped La_2MgZrO_6 and $Cs_2AgInCl_6$ NIR phosphors with double-perovskite structures also display considerable broad-band emission under an induced wave-length of 460 and 760 nm, respectively.[30,31] Yao *et al.* improved not only the internal quantum efficiency (IQE) of $LiScP_2O_7:Cr^{3+}$ from 38% to 74% but also the FWHM from 170 nm to 210 nm by Yb^{3+} codoping.[32] By means of adding fluxes and sintering in a reducing atmosphere, the $Ca_3Sc_2Si_3O_{12}:Cr^{3+}$ NIR phosphor manifests the highest IQE of ~92.3% and an excellent thermal stability of ~97.4% and the NIR emission intensity at room temperature can be maintained at 150 °C.[33] Meanwhile, the practicability of Cr^{3+}-doped phosphors in temperature sensing, infrared imaging, non-invasive detection and food quality assessment has been illustrated preliminarily.[7,34–36] Broad-band near-infrared fluorescence that can penetrate biological tissues has also been realized using $Ca_2LuHf_2Al_3O_{12}:Cr^{3+}$ and $ScBO_3:Cr^{3+}$ phosphors;[6,7] so novel NIR phosphors activated by Cr^{3+} ions are still generally regarded as important materials.

To acquire broad-band NIR spectrum in a single-phase matrix, multiple crystallographic site occupation by activators is considered as a simple but effective method.[28,36–38] In this work, the Cr^{3+}-activated $MgTa_2O_6$ phosphor was successfully synthesized by considering that the radius of Mg^{2+} (0.72 nm, CN = 6) and Ta^{5+} (0.64 nm, CN = 6) was close to that of Cr^{3+} (0.615 nm, CN = 6). As a result, a wide emission spectrum of $MgTa_2O_6:0.021Cr^{3+}$ with a large FWHM of 140 nm was observed upon 460 nm excitation. The photoluminescence mechanism was discussed in detail through the combination of the crystal structure and luminescence properties, and the two-site Cr^{3+} occupation in $MgTa_2O_6:Cr^{3+}$ phosphors accounts for the broad-band emission. Finally, a NIR pc-LED was fabricated with an $MgTa_2O_6:0.021Cr^{3+}$ phosphor pumped by a blue LED chip. Benefitting from the deep penetration of this NIR light into tissues, the visualization of blood vessels and bones in human palm and wrist is realized with the assistance of a NIR camera, suggesting its potential application in the biomedical field.

2. Experimental

2.1 Materials and preparation

Powder samples with compositions of $Mg_{1-0.67x}Ta_{2-0.33x}O_6:xCr^{3+}$ ($0 \le x \le 0.210$) (also abbreviated as $MgTa_2O_6:xCr^{3+}$ hereafter) were designed for the conservation of charge and sites and prepared by the conventional solid-state method in air. The stoichiometric starting materials, including $4MgCO_3{\cdot}Mg(OH)_2{\cdot}4H_2O$ (99.99%, Aladdin), Ta_2O_5 (99.99%, Aladdin) and Cr_2O_3 (99.95%, Aladdin), were weighed according to the given stoichiometric ratio, mixed and ground homogeneously in an agate mortar for 30 minutes. After that, the mixtures were transferred into a corundum crucible and put into a muffle furnace to sinter at 1450 °C for 6 h. At last, the furnace was cooled down to room temperature naturally and the samples were ground into fine powders for subsequent characterization.

2.2 Characterization

The phase and purity of the as-prepared powder samples were examined by X-ray diffraction (XRD) analysis using a Bruker D8 ADVANCE power diffractometer with CuKα radiation source (λ = 0.15406 nm) and a linear VANTEC detector. The operation voltage and current were set as 40 kV and 15 mA, respectively. The data were collected in the range of 5°–120° with a step size of 0.0217 nm (2θ) and a count time of 5 s per step. Structural characterization and Rietveld refinement were conducted using TOPAS 4.2 software. Room-temperature photoluminescence (PL) spectra and PL excitation (PLE) spectra were recorded using a FLS920 fluorescence spectrophotometer equipped with a continuous xenon lamp (450 W) as an excitation source and a liquid-nitrogen cooled NIR photomultiplier tube as a detector. The excitation and emission slits were both set at 2.5 nm. The PL decay curve was also measured by the same FLS920 instrument using a microsecond flash lamp (μF900) as the excitation source, and the statistical photons are 5000. Photographs for the application of NIR pc-LEDs were taken by using a DF3 NIR camera produced by Hualai Technology Company, China.

3. Results and discussion

3.1 Phase identification and structural characterization

The XRD patterns of $MgTa_2O_6:xCr^{3+}$ (x = 0.009–0.210) in Fig. 1a revealed that all diffraction peaks can be exactly assigned to the standard data of the $MgTa_2O_6$ phase (PDF No. 32-0631), indicating that the introduction of Cr^{3+} ions had no significant effect on the structure of host materials. The Rietveld refinement results of $MgTa_2O_6:0.021Cr^{3+}$ shown in Fig. 1b also verify that the phase is pure and the same crystal lattice with rutile (TiO_2) is retained. The main crystallographic data and residual factors are listed in Table 1, also corresponding to the previous report.[39]

It is reasonable to speculate that three Cr^{3+} ions tend to co-substitute two Mg^{2+} ions and one Ta^{5+} ion *via* the model of $2Mg^{2+} + Ta^{5+} \rightarrow 3Cr^{3+}$ without causing any charge or site imbalance, as also confirmed by the absence of impure phases in all samples even with high Cr^{3+} doping contents. However, the substitution mechanisms which include oxygen vacancy formations are probable also: $2Mg^{2+} + (1+n)Ta^{5+} + nO^{2-} \rightarrow (3+n)Cr^{3+} + n\text{Vacancy}(O^{2-})$ (n = 1, 2, 3...N). The suggested mechanism (n = 0) implies the smallest amount of Cr^{3+} in Ta^{5+} sites, meaning that Cr^{3+} ions prefer to occupy Mg^{2+} sites. In this case the Mg–O bond length should change more prominently than that of Ta–O under increasing Cr^{3+} doping. As the ionic radius of Cr^{3+} (0.615 nm, CN = 6) is 14.6% and 3.9% smaller than that of Mg^{2+} (0.72 nm, CN = 6) and Ta^{5+} (0.64 nm, CN = 6) respectively, the cell volume and average Mg–O bond length should decrease dramatically with the increase of Cr^{3+} concentration. But the Ta–O bond length remains almost constant.[40]

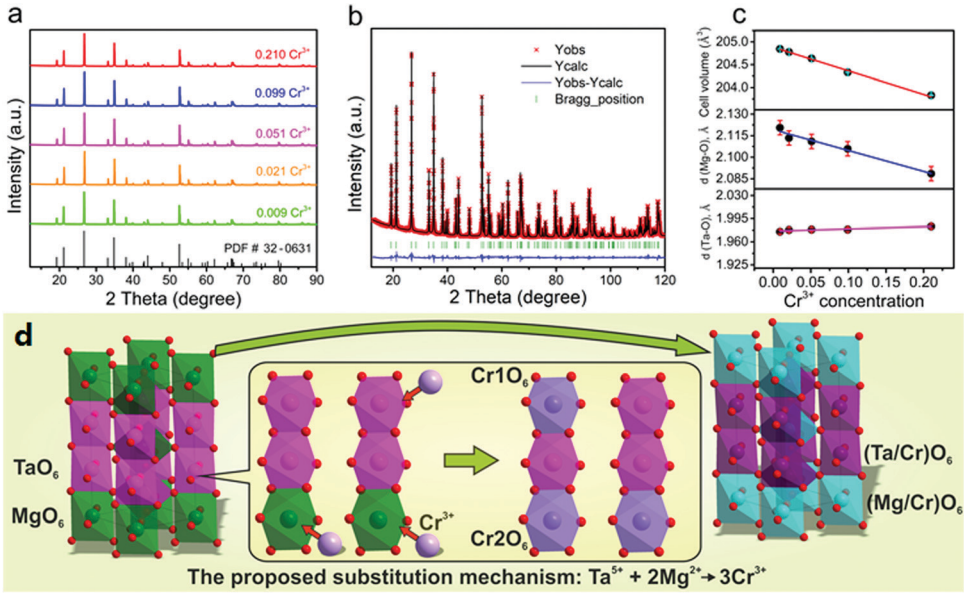

Fig. 1 (a) XRD patterns of $MgTa_2O_6$:xCr^{3+} (x = 0.009–0.210), and the standard data of $MgTa_2O_6$ phase (PDF # 32-0631). (b) Rietveld refinement XRD pattern of $MgTa_2O_6$:0.021Cr^{3+}. (c) Variation of cell volume, Mg–O bond length and Ta–O bond length with Cr^{3+} concentration, respectively. (d) Local structure evolution model demonstrating Cr^{3+} co-substituted for Mg^{2+} and Ta^{5+} in $MgTa_2O_6$.

Table 1 Main refined structural parameters of the $MgTa_2O_6$:0.021Cr^{3+} sample

Compound	$MgTa_2O_6$:0.021Cr^{3+}
Symmetry	Tetragonal
Space group	$P4_2/mnm$
a, Å	4.71649 (3)
c, Å	9.20595 (6)
V, Å^3	204.789 (3)
Z	2
2θ-interval, °	12–120
R_{wp}, %	4.09
R_p, %	3.02
R_{exp}, %	1.10
R_B, %	0.87
χ^2	3.73

These results are consistent with the results of the variations of the cell volume and the proposed doping mechanism (n = 0), Mg–O bond length and Ta–O bond length obtained by the Rietveld refinement, as shown in Fig. 1c. Fig. 1d displays the structure model of $MgTa_2O_6$ and two-site Cr^{3+} doping evolution, in particular, it consists of two distinct cationic crystallographic positions of Mg^{2+} and Ta^{5+} and both are located in the center of the distorted octahedron coordinated by six oxygen ions. Two kinds of six-coordinated Cr^{3+} ions denoted as Cr1 and Cr2 occupy Ta and Mg crystallographic sites, respectively. At the same time, the original octahedra changed a lot and caused the shrinkage of the cell volume. Interestingly, the sites of Mg are half less than those of Ta in $MgTa_2O_6$ but are occupied by more Cr^{3+} ions, which means that the Cr2 holds four times higher occupancy than Cr1. In addition to the structural information, the optical performance of the phosphor also confirmed the process of co-substitution and will be discussed later.

3.2 Optical properties

The fundamental luminescence properties of $MgTa_2O_6$:0.021Cr^{3+} were investigated using the photoluminescence (PL) and PL excitation (PLE) spectra. As shown in Fig. 2a, the PL spectrum shows a wide emission band extending from 700 to 1150 nm and centered at 834 nm with a full width at half maximum (FWHM) of 140 nm upon 460 nm irradiation, which should be attributed to the spin-allowed transition of Cr^{3+} ions from the excited state $^4T_2$ (^4F) to the ground state $^4A_2$ (^4F) as described in Fig. 2b.[41] The PLE spectrum monitored at 834 nm consists of three typical wide excitation bands located in the ultraviolet, blue and red regions, which originate from three spin-allowed transitions of $^4A_2 \rightarrow {}^4T_1$ (^4P), $^4A_2 \rightarrow {}^4T_1$ (^4F) and $^4A_2 \rightarrow {}^4T_2$ (^4F) of Cr^{3+} ions, respectively.[42] Furthermore, the PL intensity of the $MgTa_2O_6$:xCr^{3+} (x = 0.003–0.210) samples is depicted in Fig. 2c under 460 nm excitation. Obviously, the PL intensity reaches maximum when x is 0.021, and then decreases gradually due to the concentration quenching effect, which involves a non-radiative process.[43] Consequently, $MgTa_2O_6$:0.021Cr^{3+} is selected as the optimum composition for further characterization.

Given that the valence electrons of Cr^{3+} ions are not shielded by outer shells, there are strong interactions with the crystal field and lattice vibrations due to the spatial extension of the d electron wavefunctions in crystals, giving rise to tunable optical properties of Cr^{3+} doped phosphors.[44,45] When considering Cr^{3+} ions in the center of coordinated octahedra (O_h symmetry), the influence of the host lattice on luminescence properties can be expressed by the spectroscopic parameters of D_q and B, which can be roughly estimated by the following equations:[46]

$$D_q = \frac{E(^4T_2)}{10} \quad (1)$$

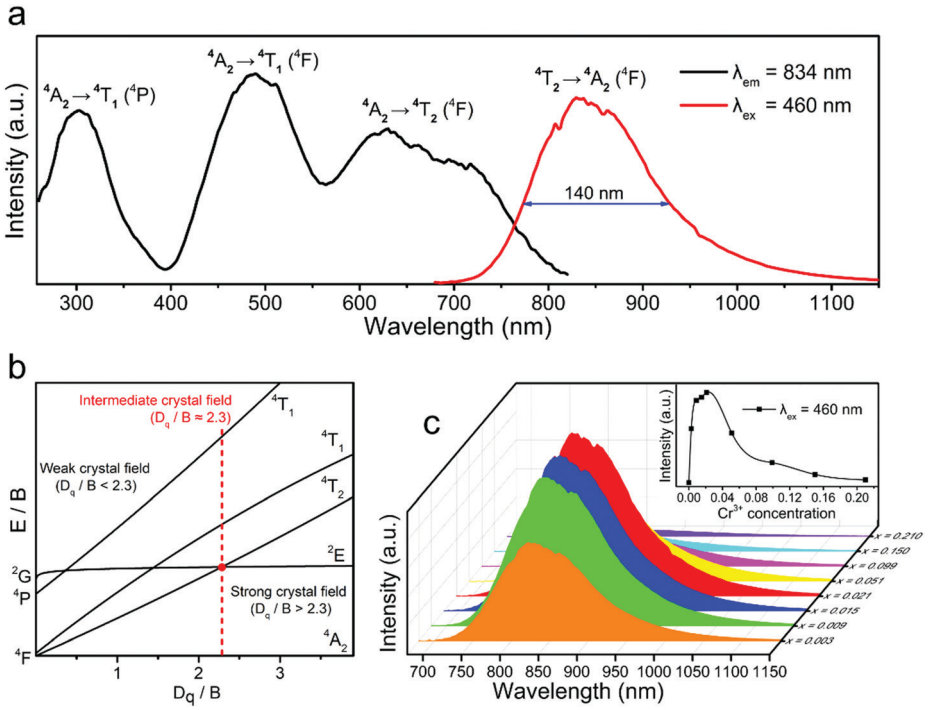

Fig. 2 (a) Room-temperature PLE and PL spectra of $MgTa_2O_6$:0.021Cr^{3+}. (b) Tanabe–Sugano diagram of d^3 electronic configuration. (c) PL spectra of $MgTa_2O_6$:xCr^{3+} ($0 \leq x \leq 0.210$) phosphors monitored at 460 nm. The inset shows the PL maximum intensity.

$$B = D_q \frac{x^2 - 10x}{15(x - 8)} \quad (2)$$

where parameter x is defined as

$$x = \frac{E(^4T_1) - E(^4T_2)}{D_q} \quad (3)$$

In the above equations, D_q is the crystal field splitting energy and is closely related to the metal–ligand distance, Racah parameter B represents the repulsive force between electrons in the 3d orbital and reveals a stronger dependence on host covalency,[48] and $E(^4T_1)$ and $E(^4T_2)$ are the equilibrium positions of the $^4T_1$ and $^4T_2$ levels, which can be obtained from the PLE spectrum shown in Fig. 2a.

Accordingly, the specific crystal field parameters of $MgTa_2O_6$:0.021Cr^{3+} were calculated and compared with those of other Cr^{3+}-doped NIR phosphors, as listed in Table 2. The crystal field strength of Cr^{3+} in $MgTa_2O_6$ is close to that in certain garnet and perovskite oxides, but larger than the crossover point in Fig. 2b, which may be ascribed to the distortion of the coordinate polyhedron because the energy level in the Tanabe–Sugano diagram is based on Cr^{3+} in a nearly perfect octahedral site.[40,47]

Table 2 Crystal field parameters of different Cr^{3+}-doped broadband NIR phosphors

Host	D_q (cm^{-1})	B (cm^{-1})	D_q/B	Ref.
$Y_3Sc_2Ga_3O_{12}$	1587	635	2.50	44
$Y_2CaAl_4SiO_{12}$	1647	678	2.43	40
$Mg_4Ga_4Ge_3O_{16}$	1695	712	2.38	27
La_2MgZrO_6	1589	628	2.53	30
$Na_2CaTi_2Ge_3O_{12}$	1538	582	2.64	47
$ScBO_3$	1400	651	2.15	13
$MgTa_2O_6$	1471	588	2.50	This work

To obtain the specific occupancy information of Cr^{3+} ions in $MgTa_2O_6$, PL Gaussian fitting has been performed as shown in Fig. 3a. Two fitting peaks are located at 834 and 910 nm with a FWHM of 124 and 197 nm, respectively. Based on the Tanabe–Sugano diagram in Fig. 2b, a wider emission spectrum and longer emission wavelength are normally relevant to a weaker crystal field, thus fitting band II (910 nm) is caused by the Cr^{3+} ions in the weaker crystal field, which is characterized by the smaller crystal field splitting.[43] Furthermore, crystal field splitting energy D_q is given by the following equation:[49]

$$D_q = \frac{ze^2r^4}{6R^5} \quad (4)$$

where z is the anion charge, e is the charge of the electron, r represents the radius of the d wave function, and R is the distance between the central Cr^{3+} ions and their ligands. Obviously, D_q strongly depends on the ligand–Cr^{3+} distance. Therefore, Cr^{3+} ions in the Mg^{2+} sites will display a longer emission wavelength.[50]

In addition, as shown in Fig. 3b, the PL intensity of single band II first reaches maximum with the increment of Cr^{3+} concentration compared to band I, which means that the luminescence center of band II is identical with stronger concentration quenching effect and higher occupancy than band I.[36] Hence the emission peaks at 834 and 910 nm were ascribed to Cr1 and Cr2, respectively. In addition, the PLE

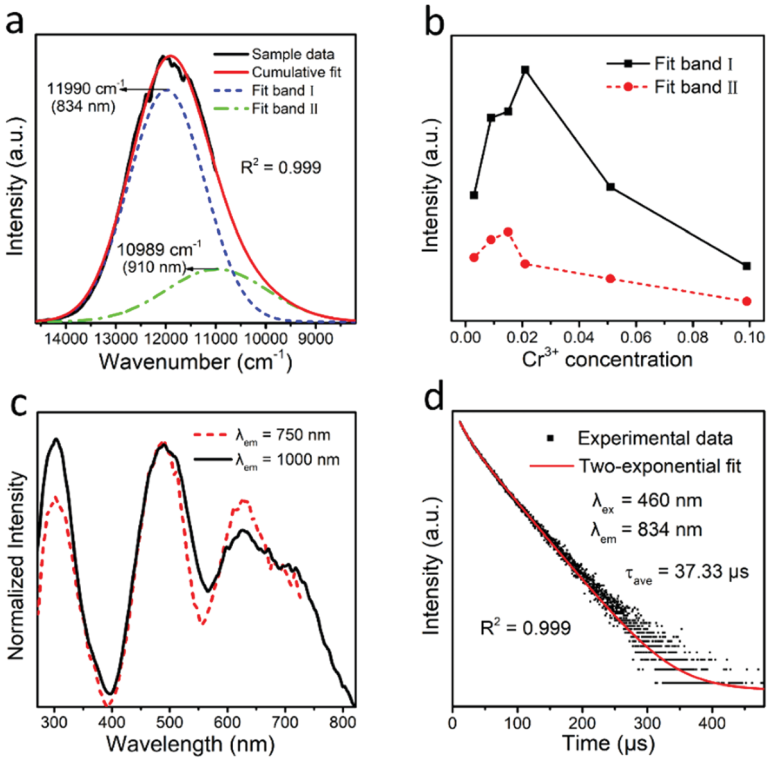

Fig. 3 (a) Gaussian fitting for the PL spectrum of the $MgTa_2O_6$:0.021Cr^{3+} phosphor. (b) PL intensity of the two fitting bands (834 and 910 nm) with Cr^{3+} concentration dependence. (c) PLE spectra of $MgTa_2O_6$:0.021Cr^{3+} monitored at 750 and 1000 nm, respectively. (d) Decay curve of $MgTa_2O_6$:0.021Cr^{3+} monitored at 834 nm.

spectra of $MgTa_2O_6$:0.021Cr^{3+} monitored at 750 and 1000 nm are displayed in Fig. 3c. The significant difference between the two curves further proves that there are two luminescence centers in this crystal.[30] Since the inhomogeneous emission band is not originated merely from one equivalent site, further evidence is revealed by checking the decay time. The decay curve of $MgTa_2O_6$:0.021Cr^{3+} monitored at the peak maximum of 834 nm upon 460 nm excitation was recorded and is shown in Fig. 3d. The average lifetime was calculated to be 37.33 μs by double-exponential fitting based on the following relationships:

$$I = A_1 e^{-\frac{t}{\tau_1}} + A_2 e^{-\frac{t}{\tau_2}} \quad (5)$$

$$\tau_{ave} = \frac{A_1\tau_1^2 + A_2\tau_2^2}{A_1\tau_1 + A_2\tau_2} \quad (6)$$

where I represents the emission intensity, A_1 and A_2 are constants, τ_1 and τ_2 are the decay time for the exponential

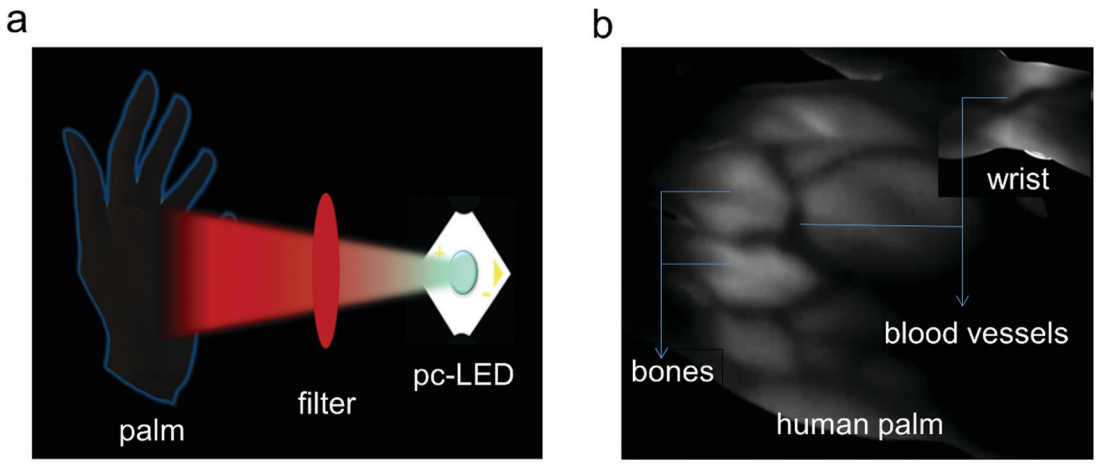

Fig. 4 (a) Schematic diagram of the NIR pc-LED imaging device showing the application principle. (b) Photographs of human palm and wrist after being penetrated by the light of $MgTa_2O_6$:0.021Cr^{3+} phosphor from the NIR pc-LED.

components, and τ_{ave} is the average decay time. The fitting results (τ_1 = 43 μs and τ_2 = 13 μs) are in line with the typical Cr^{3+}-doped compounds.[51,52]

3.3 NIR pc-LED and its applications

As mentioned previously, the broad-band NIR emission in the range of 700–1150 nm will bring about considerable penetrability to biotissues, and $MgTa_2O_6$:0.021Cr^{3+} with such a characteristic spectrum can have an effect. Therefore, a NIR pc-LED was fabricated by coating the $MgTa_2O_6$:0.021Cr^{3+} phosphor on a commercial blue light-emitting InGaN chip (460 nm). Fig. 4a shows the schematic diagram of the NIR pc-LED imaging device and a filter was used to block the faint blue light. The distribution of bones and blood vessels in human palm (~3 cm) as well as wrist (~4 cm) is observed with the assistance of a NIR camera and is shown in Fig. 4b. These images with a fundamental model indicate that the phosphor can be potentially applied for accurate measurements in non-destructive examination.

4. Conclusions

In summary, a novel Cr^{3+}-activated $MgTa_2O_6$ phosphor with broadband NIR emission has been designed based on the strategy of multiple site occupation. The $MgTa_2O_6$:0.021Cr^{3+} phosphor exhibits an asymmetric emission band in the range of 700–1150 nm with a FWHM of 140 nm upon 460 nm excitation. Experimental studies of structural characterization and optical properties reveal that the broadband emission is composed of two peaks centered at 834 and 910 nm, which are ascribed to the presence of Cr^{3+} ions in different crystallographic sites of Ta and Mg, respectively. Besides, the double site occupation of Cr^{3+} ions in $MgTa_2O_6$ was further confirmed using the PLE spectra monitored at different wavelengths and the two-exponential decay curves of luminous intensity. A NIR pc-LED was fabricated to record the distribution of human blood vessels and bones in human palm and wrist. This work provides a feasible strategy to design phosphors for broad NIR emission and to promote their potential applications in different fields.

Conflicts of interest

There are no conflicts to declare.

Acknowledgements

The present work was supported by the National Natural Science Foundations of China (Grant No. 51972118, 51961145101 and 51722202), Fundamental Research Funds for the Central Universities (D2190980), the Guangzhou Science & Technology Project (202007020005), the Guangdong Provincial Science & Technology Project (No. 2018A050506004), and the Local Innovative and Research Teams Project of Guangdong Pearl River Talents Program (2017BT01X137). This work is also funded by RFBR according to the research project No. 19-52-80003.

Notes and references

1 E. Pérez-Cabré, M. Millán and B. Javidi, *Opt. Express*, 2007, **15**, 15615–15627.
2 A. Guelpa, F. Marini, A. Plessis, R. Slabbert and M. Manley, *Food Control*, 2017, **73**, 1388–1396.
3 C. Rogel-Castillo, R. Boulton, A. Opastpongkarn, G. Huang and A. Mitchell, *J. Agric. Food Chem.*, 2016, **64**, 5958–5962.
4 J. Qiao, G. Zhou, Y. Zhou, Q. Zhang and Z. Xia, *Nat. Commun.*, 2019, **10**, 5267.
5 S. Liu, Z. Wang, H. Cai, Z. Song and Q. Liu, *Inorg. Chem. Front.*, 2020, **7**, 1467–1473.
6 M. Fang, P. Huang, Z. Bao, N. Majewska, T. Leśniewski, S. Mahlik, M. Grinberg, G. Leniec, S. M. Kaczmarek, C. Yang, K. Lu, H. Sheu and R. Liu, *Chem. Mater.*, 2020, **32**, 2166–2171.
7 L. Zhang, D. Wang, Z. Hao, X. Zhang, G. Pan, H. Wu and J. Zhang, *Adv. Opt. Mater.*, 2019, **7**, 1900185.
8 D. Hayashi, A. Dongen, J. Boerekamp, S. Spoor, G. Lucassen and J. Schleipen, *Appl. Phys. Lett.*, 2017, **110**, 233701.
9 M. Lukovic, V. Lukovic, I. Belca, B. Kasalica, I. Stanimirovic and M. Vicic, *J. Eur. Opt. Soc. - Rapid Publ.*, 2016, **12**, 19.
10 A. Zampetti, A. Minotto and F. Cacialli, *Adv. Funct. Mater.*, 2019, **29**, 1807623.
11 V. Rajendran, H. Chang and R. Liu, *Opt. Mater. Express*, 2019, **1**, 100011.
12 V. Rajendran, T. Lesniewski, S. Mahlik, M. Grinberg, G. Leniec, S. M. Kaczmarek, W. Pang, Y. Lin, K. Lu, C. Lin, H. Chang, S. Hu and R. Liu, *ACS Photonics*, 2019, **6**, 3215–3224.
13 Q. Shao, H. Ding, L. Yao, J. Xu, C. Liang and J. Jiang, *RSC Adv.*, 2018, **8**, 12035–12042.
14 P. Xiong, M. Peng, K. Qin, F. Xu and X. Xu, *Adv. Opt. Mater.*, 2019, **7**, 1901107.
15 X. Wang, Q. Liu, Y. Bu, C. Liu, T. Liu and X. Yan, *RSC Adv.*, 2015, **5**, 86219–86236.
16 S. Nishimura, S. Fuchi and Y. Takeda, *J. Mater. Sci.: Mater. Electron.*, 2017, **28**, 7157–7162.
17 B. Malysa, A. Meijerink and T. Jüstel, *Opt. Mater.*, 2018, **85**, 341–348.
18 F. Liu, Y. Liang, Y. Chen and Z. Pan, *Adv. Opt. Mater.*, 2016, **4**, 562–566.
19 E. Song, X. Jiang, Y. Zhou, Z. Lin, S. Ye, Z. Xia and Q. Zhang, *Adv. Opt. Mater.*, 2019, **7**, 1901105.
20 J. Du, O. Clercq, K. Korthout and D. Poelman, *Materials*, 2017, **10**, 1422.
21 M. Peng, B. Sprenger, M. Schmidt, H. Schwefel and L. Wondraczek, *Opt. Express*, 2010, **18**, 12852–12863.
22 J. Cao, J. Peng, L. Wang, H. Luo, X. Wang, P. Xiong, Y. Wang and M. Peng, *J. Mater. Chem. C*, 2019, **7**, 2076–2084.
23 R. Zou, S. Gong, J. Shi, J. Jiao, K. Wong, H. Zhang, J. Wang and Q. Su, *Chem. Mater.*, 2017, **29**, 3938–3946.

24 S. Möller, A. Katelnikovas, M. Haase and T. Jüstel, *J. Lumin.*, 2016, **172**, 185–190.
25 Q. Bai, S. Zhao and L. Guan, *et al.*, *Cryst. Growth Des.*, 2018, **18**, 3178–3186.
26 Z. Pan, Y. Lu and F. Liu, *Nat. Mater.*, 2011, **11**, 58–63.
27 Y. Zhan, Y. Jin, H. Wu, L. Yuan, G. Ju, Y. Lv and Y. Hu, *J. Alloys Compd.*, 2019, **777**, 991–1000.
28 X. Xu, Q. Shao, L. Yao, Y. Dong and J. Jiang, *Chem. Eng. J.*, 2020, **383**, 123108.
29 V. Rajendran, M. Fang, G. Guzman, T. Lesniewski, S. Mahlik, M. Grinberg, G. Leniec, S. M. Kaczmarek, Y. Lin, K. Lu, C. Lin, H. Chang, S. Hu and R. Liu, *ACS Energy Lett.*, 2018, **3**, 2679–2684.
30 H. Zeng, T. Zhou, L. Wang and R. Xie, *Chem. Mater.*, 2019, **31**, 5245–5253.
31 F. Zhao, Z. Song, J. Zhao and Q. Liu, *Inorg. Chem. Front.*, 2019, **6**, 3621–3628.
32 L. Yao, Q. Shao, S. Han, C. Liang, J. He and J. Jiang, *Chem. Mater.*, 2020, **32**, 2430–2439.
33 Z. Jia, C. Yuan, Y. Liu, X.-J. Wang, P. Sun, L. Wang, H. Jiang and J. Jiang, *Light: Sci. Appl.*, 2020, **9**, 86.
34 J. Yang, Y. Liu, Y. Zhao, Z. Gong, M. Zhang, D. Yan, H. Zhu, C. Liu, C. Xu and H. Zhang, *Chem. Mater.*, 2017, **29**, 8119–8131.
35 R. Zou, J. Huang, J. Shi, L. Huang, X. Zhang, K. Wong, H. Zhang, D. Jin, J. Wang and Q. Su, *Nano Res.*, 2017, **10**, 2070–2082.
36 C. Wang, X. Wang, Y. Zhou, S. Zhang, C. Li, D. Hu, L. Xu and H. Jiao, *ACS Appl. Electron. Mater.*, 2019, **1**, 1046–1053.
37 H. Lin, G. Bai, T. Yu, M. Tsang, Q. Zhang and J. Hao, *Adv. Opt. Mater.*, 2017, **5**, 1700227.
38 L. Zhang, S. Zhang, Z. Hao, X. Zhang, G. Pan, Y. Luo, H. Wu and J. Zhang, *J. Mater. Chem. C*, 2018, **6**, 4967–4976.
39 G. Halle and H. Mueller-Buschbaum, *J. Less-Common Met.*, 1988, **142**, 263–268.
40 M. Mao, T. Zhou, H. Zeng, L. Wang, F. Huang, X. Tang and R. Xie, *J. Mater. Chem. C*, 2020, **8**, 1981–1988.
41 M. Back, E. Trave, J. Ueda and S. Tanabe, *Chem. Mater.*, 2016, **28**, 8347–8356.
42 D. Dai, Z. Wang, Z. Xing, X. Li, C. Liu, L. Zhang, Z. Yang and P. Li, *J. Alloys Compd.*, 2019, **806**, 926–938.
43 T. Gao, W. Zhuang, R. Liu, Y. Liu, C. Yan, J. Tian, G. Chen, X. Chen, Y. Zheng and L. Wang, *J. Am. Ceram. Soc.*, 2019, **103**, 202–213.
44 B. Malysa, A. Meijerink and T. Jüstel, *J. Lumin.*, 2018, **202**, 523–531.
45 X. Meng, Z. Wang, K. Qiu, Y. Li, J. Liu, Z. Wang, S. Liu, X. Li, Z. Yang and P. Li, *Cryst. Growth Des.*, 2018, **18**, 4691–4700.
46 J. Perumareddi, *Coord. Chem. Rev.*, 1969, **4**, 73–105.
47 X. Zhou, G. Ju, T. Dai and Y. Hu, *Opt. Mater.*, 2019, **96**, 109322.
48 A. Trueba, P. Garcia-Fernandez, J. Garcia-Lastra, J. Aramburu, M. Barriuso and M. Moreno, *J. Phys. Chem. A*, 2011, **115**, 1423–1432.
49 Z. Ming, J. Qiao, M. S. Molokeev, J. Zhao, H. C. Swart and Z. Xia, *Inorg. Chem.*, 2020, **59**, 1405–1413.
50 J. Yuan, Y. Zhang, J. Xu, T. Tian, K. Luo and L. Huang, *J. Alloys Compd.*, 2019, **815**, 152656.
51 B. Malysa, A. Meijerink, W. Wu and T. Jüstel, *J. Lumin.*, 2017, **190**, 234–241.
52 X. Wu, D. Xu, W. Li, T. Wang, L. Cao and J. Meng, *Luminescence*, 2017, **32**, 1554–1560.

